Corrosion Science 171 (2020) 108658

Contents lists available at ScienceDirect

Corrosion Science

journal homepage: www.elsevier.com/locate/corsci

Surface and corrosion properties of AA6063-T5 aluminum alloy in molybdate-containing sodium chloride solutions

Dmitry S. Kharitonov[a,b,c,*,1], Illia Dobryden[a,**], Birhan Sefer[d,e], Jacek Ryl[f], Angelika Wrzesińska[g], Irina V. Makarova[h], Izabela Bobowska[g], Irina I. Kurilo[i], Per M. Claesson[a,j]

[a] Division of Surface and Corrosion Science, Department of Chemistry, School of Engineering Sciences in Chemistry, Biotechnology and Health, KTH Royal Institute of Technology, SE-100 44 Stockholm, Sweden
[b] Department of Chemistry, Electrochemical Production Technology and Materials for Electronic Equipment, Chemical Technology and Engineering Faculty, Belarusian State Technological University, 220006 Minsk, Belarus
[c] Jerzy Haber Institute of Catalysis and Surface Chemistry, Polish Academy of Sciences, 30-239 Krakow, Poland
[d] Division of Materials Science, Department of Engineering Sciences and Mathematics, Luleå University of Technology, SE-97187 Luleå, Sweden
[e] Metallic Materials in Corrosive Environments, Swerim AB, Box 7047, SE-16407 Kista, Sweden
[f] Department of Electrochemistry, Corrosion and Materials Engineering, Gdansk University of Technology, 80-233 Gdansk, Poland
[g] Department of Molecular Physics, Lodz University of Technology, 90-924 Lodz, Poland
[h] Department of Separation and Purification, School of Engineering Science, Lappeenranta University of Technology, FI-53850 Lappeenranta, Finland
[i] Department of Physical, Colloid and Analytical Chemistry, Organic Substances Technology Faculty, Belarusian State Technological University, 220006 Minsk, Belarus
[j] RISE Research Institutes of Sweden, Chemistry, Materials and Surfaces, SE-114 86 Stockholm, Sweden

ARTICLE INFO

Keywords:
Aluminum
Raman spectroscopy
SEM
XPS
Scanning probe microscopy
Molybdate inhibitor

ABSTRACT

Corrosion properties of aluminum alloy AA6063-T5 were investigated in molybdate-containing NaCl solutions. Electrochemical, microscopic, and spectroscopic experiments were utilized to examine the mechanism of corrosion inhibition by molybdates. SEM-EDX, magnetic force, and intermodulation electrostatic force microscopy data suggested that the inhibition initiation preferentially occurred over Fe-rich cathodic IMPs. Spectroscopic measurements demonstrated that the formed surface layer consists of mixed Mo(VI, V, IV) species. This layer provided inhibition with an efficiency of ~90% after 4 h of exposure. High efficacy of ~70% was achieved even after one week of exposure. A two-step oxidation-reduction mechanism of corrosion inhibition by aqueous molybdates was proposed.

1. Introduction

Corrosion phenomena are among the key reasons for reduced lifetime and early failure of metallic-based components and structures in daily life applications and technologies. Aluminum alloys are frequently used and they suffer from corrosion. The rather high corrosion resistance of pure Al is due to the spontaneously formed compact and adherent oxide film [1,2]. However, in the case of Al alloys, the surface layer contains many heterogeneities, such as intermetallic particles (IMPs) [3]. These IMPs form local anodes or cathodes in the material microstructure, and thus increase the susceptibility for localized corrosion [3–5]. This makes corrosion protection of Al alloys a critical issue and requires development of various protection strategies.

Utilization of corrosion inhibitors is a commonly used approach to prevent corrosion of metallic materials. A successful inhibitor for Al alloys is chromate due to its versatility, high inhibition efficiency, and self-healing ability [6,7]. However, chromates are carcinogens and mutagens. Thus, attention has recently been given to the development of new environmentally friendly and efficient inhibitor alternatives. In this context, oxyanions of the transition metals from the VB–VIIB groups of the periodic table have been extensively examined [8–10]. Among them, molybdates and vanadates showed the strongest potential to effectively reduce the corrosion rate of Al alloys [9,11–13]. From the environmental point of view, molybdates are more promising due to their lower toxicity [14]. A protective ability of molybdates towards pure aluminum [15,16], which was not observed for vanadates, also

* Corresponding author at: Jerzy Haber Institute of Catalysis and Surface Chemistry, Polish Academy of Sciences, 30-239 Krakow, Poland
** Corresponding author at: Division of Surface and Corrosion Science, Department of Chemistry, School of Engineering Sciences in Chemistry, Biotechnology and Health, KTH Royal Institute of Technology, SE-100 44 Stockholm, Sweden.
E-mail addresses: nckharyt@cyf-kr.edu.pl (D.S. Kharitonov), illia@kth.se (I. Dobryden).
[1] Authors contributed equally to this work.

https://doi.org/10.1016/j.corsci.2020.108658
Received 25 December 2019; Received in revised form 4 March 2020; Accepted 6 April 2020
Available online 11 May 2020

suggests their versatility and motivates the inhibitor choice of this study.

Despite extensive knowledge of corrosion inhibition of galvanized steel and Zn by molybdates, it is less common to implement them for corrosion inhibition of Al alloys. There are many approaches to form molybdate-phosphate conversion coatings reported [11,17]. The protective action of molybdate-phosphate coatings is attributed to the formation of passive Mo–P layers, known as molybdenum blues. Recently, Huang et al. reported formation of a phosphorus-free Mo-rich conversion coating from an alkaline bath, consisting of AlF_3, Al_2O_3, MoO_3, and $Al_2(MoO_4)_3$ on AA6063 alloy [18].

The inhibition effect of soluble molybdates in corrosive media has been reported to depend on ionic strength and initial inhibitor concentration [9,15,19,20]. Several studies [16,21] have reported that molybdate can displace chloride ions from the metal-solution interface due to competitive adsorption, and this adsorbed layer will act as a protective barrier [21]. Later, a more complex mechanism was proposed [16], which includes initial adsorption of molybdate ions followed by their reduction and accompanied oxidation of Al. Most of the studies were carried out using the Al alloy AA2024. Jakab et al. analyzed cobalt-, cerium-, and molybdenum-based inhibitors and reported a high potential of molybdate for suppression of the oxygen reduction reaction (ORR) [22]. However, molybdate had the highest critical concentration. Later, Lopes-Garrity and Frankel reported the threshold concentration for the effective corrosion protection of AA2024-T3 to be 0.1 M Na_2MoO_4 [9]. They also emphasized the importance of the IMPs for the initiation of the corrosion inhibition process. For other Al alloys, containing anodic alloying elements (Mg, Zn, etc.), the exact inhibitor protection mechanism still requires a better fundamental understanding.

Accurate measurements of the potential of individual IMPs in Al alloys and the IMPs effects on the corrosion mechanism have attracted significant interest in recent studies [3,4,23]. In this work we utilize advanced scanning probe methods, such as Intermodulation electrostatic force microscopy (ImEFM [24]) and magnetic force microscopy (MFM) to gain insight into the microstructure of the AA6063-T5 alloy, and the formation of the molybdate protective layer. The ImEFM technique provides a higher lateral resolution and high potential resolution than commonly applied lift-mode techniques, such as in scanning Kelvin probe force microscopy (SKPFM) [24]. In our previous study [23] we demonstrated that ImEFM allows accurate investigations of IMPs at the nanoscale. The main focus of this study is to elucidate the corrosion inhibition efficiency of molybdates and its mechanism in aqueous NaCl medium, with a specific focus on probing nanoscale electrochemical properties of intermetallic particles and the composition of the protective layer on the AA6063-T5 alloy.

2. Experimental

2.1. Materials and sample preparation

Aluminum alloy AA6063-T5 was used as extruded plate material. The nominal chemical composition, as provided by the supplier (Taspo Radiators, Belarus), is given as (wt.%): 0.45 Si, 0.50 Fe, 0.10 Cu, 0.10 Mn, 0.60 Mg, 0.1 Cr, 0.15 Ti, and balance Al. All samples with sizes of 20 mm × 20 mm and thickness of 2.5 mm were cut from the plate material in the normal direction. The samples for the microstructure and scanning probe microscopy studies were mechanically ground to 4000-grit and polished with up to 0.25 μm diamond paste using 99.9% alcohol as a lubricant until the mirror surface finish was achieved. Before experiments, all samples were ultrasonically cleaned in 99.9% ethanol for 10 min. Electrochemical measurements were performed on samples ground to 1200-grit without further polishing.

2.2. SEM and EDX analyses

The surface morphology and elemental composition of the samples before and after the corrosion experiments were investigated by scanning-electron-microscopy imaging (SEM) and energy-dispersive X-ray (EDX) measurements using a JEOL JSM-5610LV scanning electron microscope equipped with a JEOL JED-2201 system for micro-EDX analysis.

2.3. SPM measurements

Scanning probe microscopy measurements of surface topography and contact potential voltage difference were carried out with Intermodulation Atomic Force Microscopy (ImAFM) [25] and Intermodulation Electrostatic Force Microscopy (ImEFM) [24] using a Bruker Dimension Icon AFM (Bruker). While SKPFM methods are well-established and are often used to characterize surface electrochemical properties, the ImEFM technique can offer simultaneous lateral and potential measurements with higher resolution. This can be of importance for characterizing the nanoscale interface region between IMPs and matrix. A multi-frequency lock-in amplifier (Intermodulation Products AB) was connected to an Icon AFM. The measurements were conducted in air at ambient conditions using HQ:NSC18 probes (MikroMasch) with platinum coating for local electrical measurements. The nominal tip outer radius was less than 30 nm and the nominal cantilever spring constant was 2.8 N/m. The imaging setpoint was optimized (by lowering the tip-surface interaction force) to minimize possible cross-talk between the measured topography and potential signals. The ImEFM measurements were conducted at 1 Hz acquisition speed and the resulting potential maps contain 256 × 256 data points. A tip bias of 6 V was applied for the measurements. The obtained maps of Volta potential were not inverted. Data treatment such as flattening or smoothing was not done for the Volta potential maps. The data were analyzed using the IMP software suite (version 1.1, Intermodulation AB) and the SPM images were prepared using the Gwyddion software (version 2.44). Magnetic Force Microscopy (MFM) measurements were carried out with a Dimension Icon AFM (Bruker) in a two-pass mode, i.e. topography was measured during the first pass, while the phase change due to magnetic interactions was measured above the surface during the second pass. The measurements were conducted using MESP-V2 (Bruker) probes with cobalt-chromium coating. The probes have a nominal tip outer radius of about 35 nm. The nominal cantilever spring constant was 3 N/m. The probes were magnetized using a standard probe magnetizer (Bruker) and kept in the magnetic field for about 30 s. The MFM measurements were conducted at scan rates of 0.6–1 Hz and the resulting maps contain 256 × 256 data points. The lift distance for the magnetic response measurements in the second-pass was 100 nm for the as-prepared samples (while height variation for surface features measured at the first-pass was only up to 25 nm). After the inhibitor layer was formed, the lift distance was increased to 500 nm to avoid possible cross-talk between the magnetic response and topography (in this case height variations of up to 300 nm were observed during the first-pass scanning).

2.4. Corrosion evaluation

All solutions for corrosion studies were prepared with analytical grade NaCl (≥99.5) and $(NH_4)_6Mo_7O_{24}{\cdot}4H_2O$ (≥99.98) obtained from Belreachim (Belarus), and 18.2 MΩ cm Milli-Q deionized water. Corrosion experiments were performed in 0.05 M NaCl + 3 mM $(NH_4)_6Mo_7O_{24}$ solution (pH ~7.2) without pH adjustment. The solutions were stored in closed flasks for 24 h under laboratory conditions (~20 °C) to ensure equilibration of Mo species. Reference measurements were done in 0.05 M NaCl without inhibitor. The inhibitor concentration was selected to provide a comparison of the effectiveness of molybdates with that of the vanadate inhibitor used in our previous

studies [4,12].

Electrochemical measurements comprised potentiodynamic polarization scans and electrochemical impedance spectroscopy (EIS) measurements. An Autolab PGSTAT302 N potentiostat/galvanostat and a standard three-electrode cell setup with a saturated Ag/AgCl reference electrode and a Pt-mesh counter electrode were used at room temperature (~21 °C). The exposed area of the sample was 1 cm^2 and the measurements were at least triplicated.

Potentiodynamic polarization curves were recorded within the potential range from −200 mV to +200 mV vs. open-circuit potential (OCP) at a scan rate of 0.5 mV/s. The Levenberg-Marquardt method available in the *CorrView 3.2c* software was used to extract the electrochemical parameters from polarization curves. EIS measurements were carried out at the OCP over the frequency range from 10^4 to 10^{-2} Hz using a sinusoidal perturbation amplitude of 10 mV. The *ZView 3.2* and *Nova 1.11* software were used for data analysis and spectra fitting.

Static immersion weight loss measurements were carried out for 1000 h at 25 ± 1 °C in a TC-80M-2 temperature-controlled cabinet. The exposed surface area of all samples was 5 cm^2 and the solution-to-specimen area ratio was 50 $cm^3/1\ cm^2$. The samples were taken out from the solutions at discrete time intervals, thoroughly rinsed by deionized water, dried in a desiccator, and weighed with 0.1 mg accuracy using an OHAUS PX225DM microbalance. All weight loss measurements were replicated on 5 parallel samples.

2.5. Raman spectroscopy

Raman spectra of the AA6063-T5 surface after exposure to the studied solution were acquired *ex-situ* with a Jobin-Yvon T64000 Raman spectroscopy system equipped with an Olympus BX40 confocal optical microscope with a ×50 lens (NA 0.75). The Raman spectra were excited with an Ar^+-laser at 514.5 nm with an incident power of 5 mW and an acquisition time of 600 s. The samples were rinsed with deionized water, air dried, and analyzed within 2 h upon removal from the solutions. All spectra were acquired at least in duplicate on three different spots of the sample.

2.6. X-ray photoelectron spectroscopy (XPS)

High-resolution XPS spectra of the AA6063-T5 surface were registered directly after exposure to 0.05 M NaCl +3 mM $(NH_4)_6Mo_7O_{28}$ electrolyte for 24 h using a ThermoFisher Scientific Escalab 250Xi spectrometer, equipped with an Al Kα X-Ray source (spot size 250 μm), operating at pass energy of 10 eV. The samples were rinsed with deionized water, air dried, and transferred to a vacuum chamber within 15 min upon removal from the solution. Charge compensation was provided by calibration performed for adventitious carbon at the C1s peak (BE = 284.6 eV). The *Avantage* software from ThermoFisher Scientific was used for peak deconvolution.

2.7. Calculation of molybdenum speciation in aqueous solutions

The predominance and fractional chemical equilibrium diagrams for molybdenum species in the aqueous solutions were calculated using the *Medusa* Software (KTH Royal Institute of Technology, Sweden) based on the SOLGASWATER algorithm. Thermodynamic equilibrium constants for the calculations were obtained from the embedded *Hydra* database. Calculation conditions were chosen to represent those experimentally applied.

3. Results and discussion

3.1. Surface analysis

The microstructure of as-polished AA6063-T5 is shown in Fig. 1. Numerous IMPs were observed on the alloy surface without clear tendency for clustering. The major fraction of the IMPs was found to be in the range of 3–10 μm. EDX spectra were measured on individual IMPs and away from the particles, as exemplified by the spots marked in Fig. 1c. It was found that the majority of the micrometer-sized IMPs are rich in Fe and Si, while the surface layer away from the IMPs does not contain iron (Table 1, areas 1–3). Such micrometer-sized precipitates constitute active sites for the corrosion initiation and propagation due to the local galvanic interactions caused by the difference in the electrochemical nature of IMPs and Al matrix [4,23].

A comprehensive study of AA6063-T5 alloy IMPs found at the surface were carried out using the ImEFM method. Topography, contact potential difference and magnetic force maps of such IMP are shown in Fig. 2.

A micrometer-sized secondary-phase precipitate consisting of two parts can be observed in the topography image of 20 μm × 20 μm size (Fig. 2a) and a higher resolution topography image of 6.2 μm × 6.2 μm size (Fig. 2d). The height variation along the particle and the Al matrix is only a few nm. Thus, the measured surface is well-polished with limited surface roughness, which is important since it will minimize cross-talk between potential and topography measurements in ImEFM, and between magnetic force measurements and topography in MFM. The intermetallic particle is clearly visible in the ImEFM image as it has a different contact potential difference compared to the aluminum matrix, see Fig. 2(b, e). The smaller submicron IMPs, possibly dispersoids, are clearly visible in the ImEFM map. Both of the micrometer-sized IMPs showed significantly higher (about −515 mV ± 14 mV) potentials than the surrounding Al matrix with an average potential of about −1300 mV (Fig. 2f). Thus, these two large IMPs are more electrochemically noble than the alloy matrix that suggests a high propensity for micro-galvanic corrosion around them. It is well-known that the measurement conditions such as tip probe geometry, coating material and coating quality, oxide layer thickness, as well as other precipitates and water can strongly affect the absolute contact potential values [26]. Thus, it is preferred to compare the difference between the Volta potential between IMPs and the matrix rather than the absolute values. For the particles shown in Fig. 2 the contact potential difference is 790 mV as shown in the cross-section potential data image in Fig. 2f.

Numerous submicron IMPs with lower Volta-potential differences relative to the matrix were also observed on the surface. It was previously reported that submicron-sized cathodic precipitates cannot provide sufficient driving force to support the dissolution of the surrounding anodic region, while the micrometer-sized cathodic IMPs provide sufficient driving force to cause localized corrosion [3,4,23]. The large cathodic IMP was further imaged with higher potential resolution, as shown in Fig. 2e, and the data demonstrate a clear gradient at the IMP edge. Finite element modeling has demonstrated that such IMPs and their edges can affect and drive the micro-galvanic corrosion [27]. The width of the interphase potential gradient zone was calculated to be about 770 nm ± 260 nm with a Volta-potential gradient of up to ~0.55 mV/nm. In the case of galvanic corrosion, this zone around IMPs can be considered as a corrosion initiation zone controlled by material variations.

The presence of micrometer-sized IMPs with high cathodic activity can be explained by a large fraction of electrochemically nobler (relative to Al) metals, in particular Fe, in their composition, as shown by the EDX spectra (Table 1). However, it would be beneficial to be able to distinguish IMPs of different chemical composition using only SPM techniques, as possible by using the MFM mode. Considering that large IMPs in AA6063-T5 contain a large fraction of iron, which is ferromagnetic, it seems possible to locate such IMPs. Indeed, MFM measurements identify a strong magnetic response for some IMPs in the AA6063-T5 alloy, as shown in Fig. 2c. Two IMPs of about the same shape and sizes as the particle in Fig. 2e have an increased phase value, which is attributed to the magnetic response. Thus, MFM measurements (Fig. 2c) allow identification of Fe-rich IMPs, which is consistent with the EDX spectra for similar IMPs reported in this study. The point EDX

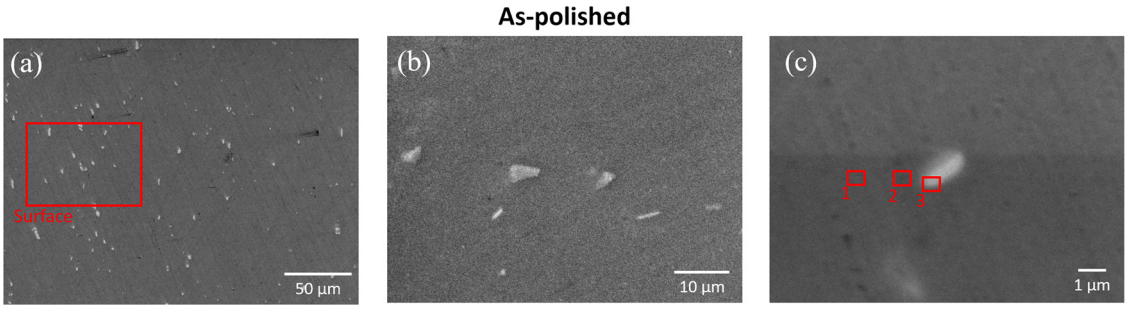

Fig. 1. SEM images of as-polished AA6063-T5 surface. Labeled regions correspond to the EDX analysis listed in Table 1.

Table 1
Elemental composition of the AA6063-T5 surfaces before and after immersion in 0.05 M NaCl solutions.

	Element, wt.%											
	Al	Fe	Si	Mg	Cr	Mn	C	Zn	Ti	Cu	Mo	O
AA6063-T5 as-polished												
Surface	98.27	0.53	0.24	0.52	0.09	0.05	–	0.17	0.09	0.04	–	–
Area 1	84.90	–	0.65	0.88	–	–	12.67	–	–	–	–	0.89
Area 2	78.50	2.42	1.99	3.82	–	–	12.52	–	–	–	–	0.75
Area 3	72.17	10.59	3.23	1.50	–	0.39	12.12	–	–	–	–	–
0.05 M NaCl												
Area 4	77.28	0.19	1.33	0.42	–	0.06	17.56	–	–	–	–	3.14
Area 5	72.50	2.97	2.66	0.40	–	0.15	18.06	–	–	–	–	3.27
Area 6	71.92	2.80	2.57	0.36	–	0.08	18.93	–	–	–	–	3.34
Area 7	74.45	2.18	0.54	–	–	–	19.05	–	–	–	–	3.78
Area 8	64.65	1.97	7.49	0.34	–	–	18.18	–	–	–	–	7.37
Area 9	96.46	1.77	–	0.61	–	–	–	–	–	–	–	1.17

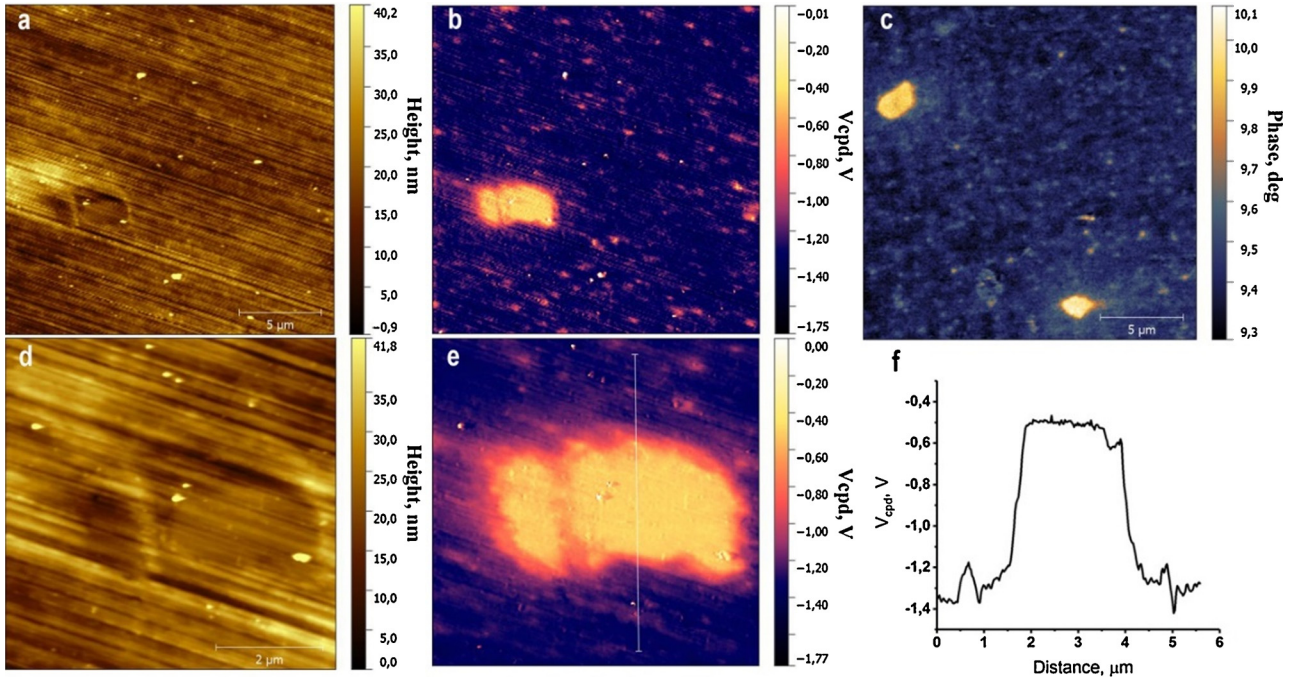

Fig. 2. Topography AFM maps (a, d) and corresponding ImEFM Volta-potential maps (b, e) showing intermetallic phases in the microstructure of AA6063-T5 surface. The line profile (f) shows the potential along the line in the corresponding map (e). MFM map in (c) shows Fe distribution over the surface. The image size was $20 \times 20\,\mu m^2$ in panels (a–c) and $6.2 \times 6.2\,\mu m^2$ in panels (d, e).

analysis of the micrometer-sized second phases shows that they are of Al-Fe-Si, Al-Mg-Fe-Si and Al-Fe type (Table 1).

3.2. Corrosion experiments

3.2.1. AA6063-T5 in absence of inhibitor

3.2.1.1. SEM/EDX analysis. A series of corrosion experiments in 0.05 M NaCl solution without the molybdate inhibitor was performed, and SEM

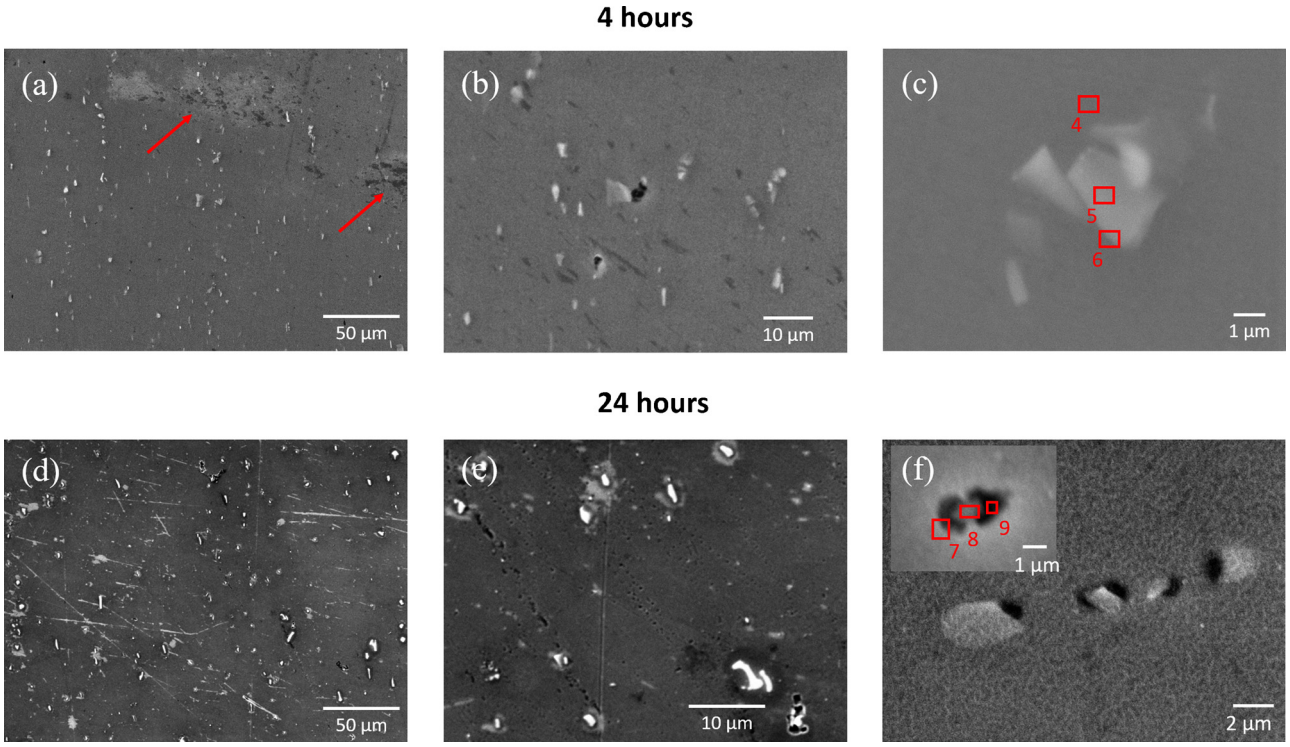

Fig. 3. SEM images of AA6063-T5 surface after 4 h (top line) and 24 h (bottom line) exposure to 0.05 M NaCl. Labeled regions correspond to the EDX analysis listed in Table 2.

micrographs of AA6063-T5 after 4 and 24 h of exposure are shown in Fig. 3. A severe corrosion attack is evident already after 4 h, and a region suffering severe general corrosion of the alloy matrix (marked with an arrow in Fig. 3a) with corrosion products covering the surface as well as localized pitting around some large IMPs were detected. However, the interface around IMPs of sub-micron and a few of 2–4 µm sizes remained almost intact. After 24 h of immersion, corrosion was even more evident. Pitting was observed around the majority of the micrometer-sized IMPs (as shown in Fig. 3f), and a thick layer of corrosion products covered the vicinity sites. The observed morphology changes provide evidence that corrosion was initiated at the IMP/matrix interface and progressed towards the alloy matrix, as suggested by the Volta-potential mapping (Fig. 2). Point EDX analysis after 4 and 24 h of exposure (Fig. 3 and Table 1) revealed some decrease in the content of Mg in the composition of IMPs, while the amount of Fe and Si remained constant. This can be caused by the selective dissolution of the more active (anodic) component (Mg) from the iron-rich IMP. This selective dissolution causes dealloying of IMPs, enriching the surface in iron and silicon. A high amount of detected oxygen supports deposition of corrosion products in the form of oxides/hydroxides on the surface.

3.2.2. *AA6063-T5 in the presence of molybdate inhibitor*

The surface morphology is clearly different in the case of AA6063-T5 alloy immersion in 0.05 M NaCl with 3 mM $(NH_4)_6Mo_7O_{24}$ inhibitor, as shown in Fig. 4. The extent of corrosion attack associated with the matrix and IMPs was lower compared to the situation without inhibitor. Furthermore, small round-shaped particles were formed on the surface (Fig. 4c), which are Mo-based oxides. The surface coverage of Mo-based oxides is not homogeneous after 4 h, but it increased significantly with time, and after 24 h an almost homogeneous distribution is observed. This is more evident in the images of higher resolution (Fig. 4(b,d)). The EDX analysis of the surface region with micrometer-sized IMP, most likely of α-Fe-Si-Al-type, revealed high content of Mo and O over this precipitate, as demonstrated in Fig. 4e. This provides evidence for the formation of a Mo-based oxide passivation layer on top of the IMP. Note that no clear sign of localized corrosion was observed around this IMP. Our data indicate that molybdate suppresses the cathodic activity of such IMPs. The cracks observed in the formed layer are likely due to internal stresses that develop as the thickness increases.

The preferential localization of Mo-based oxide on the micro-galvanic corrosion active IMPs is of high relevance and further information was gained by using the SPM methods. Topography SPM images of the alloy surface after 4 h treatment in 0.05 M NaCl with 3 mM $(NH_4)_6Mo_7O_{24}$, Fig. 5(a,d), confirm the presence of Mo-based oxide particles with sizes around 300–550 nm. The cross-section profiles over three particles are shown in Fig. 5g. Many much smaller molybdate particles are also observed in the SPM topography image, which contribute to an overall surface roughening. The topographical images do not clearly identify IMPs covered by the Mo-based oxides. However, this can be achieved using the MFM mode (Fig. 5(b,e)) where Fe-rich IMPs can be distinguished in the magnetic response maps (Fig. 2c). Indeed, a strong magnetic response was measured over the Mo-covered particles as shown in Fig. 5(b,e), and the difference relative to the matrix is illustrated by the MFM cross-section profile data reported in Fig. 5h. However, it is not trivial to distinguish if such magnetic response arises from the underlying Fe-rich IMPs or due to paramagnetic properties of the molybdenum oxides [28]. Nevertheless, this approach can indicate possible preferential inhibitor deposition over Fe-rich IMPs, and it will be useful for more clear cases in future studies.

The contact potential difference maps, Fig. 5(c,f), were recorded over the same particles after 4 h of exposure to the inhibitor-containing solution. It is evident that the potential variation between the particles and the Al matrix is much smaller than prior to immersion in the inhibitor-containing solution. The average contact potential voltage over the particle in Fig. 5f is 510 mV ± 40 mV, whereas the average contact potential voltage over the matrix area in Fig. 5(c,f) is 680 mV ± 40 mV. Thus, the difference in Volta potential between the particles and the matrix is only about 170 mV, which is approximately 5 times less than for the freshly polished Al alloy surface. The cross-section contact potential difference over the particle is shown in Fig. 5i. Our

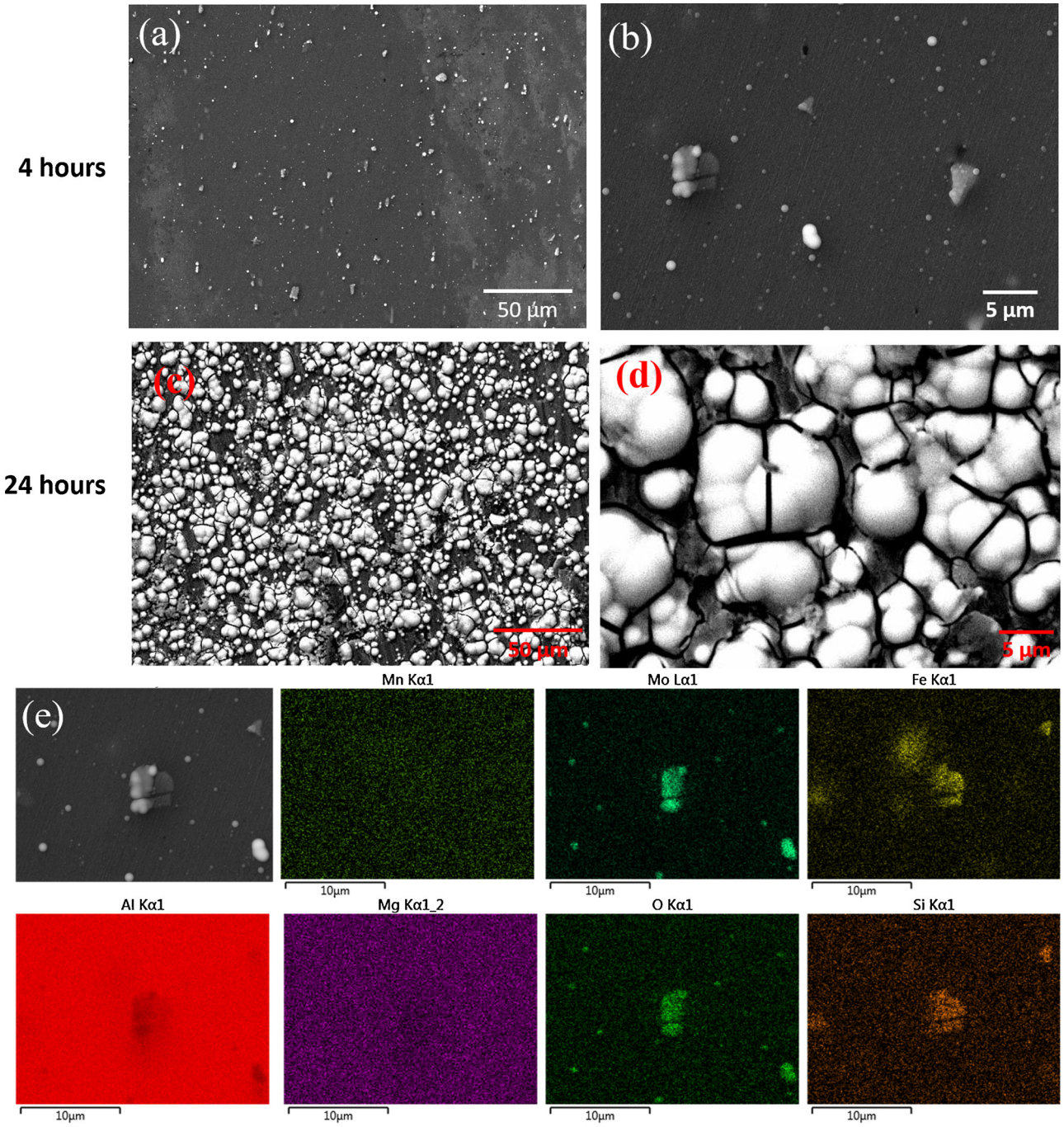

Fig. 4. SEM-EDX surface analysis after 4 and 24 h exposure to 0.05 M NaCl solution with 3 mM $(NH_4)_6Mo_7O_{24}$. (For interpretation of colours in this figure, the reader is referred to the web version of this article).

SPM data is consistent with the corrosion protection offered by the presence of the molybdate inhibitor on the surface. The small differences in Volta potential between the particle and matrix also indicate some possible effects. The presence of a thin deposited layer of molybdate oxide of varying thickness over the entire surface and IMPs may reduce the Volta potential difference observed over the IMP and the matrix. A possible underlying IMP under a molybdate oxide aggregate can additionally contribute to the measured difference in potentials. Also, the potential gradient at the particle edge region is less clear compared to that at the edge of the unexposed IMP shown in Fig. 2. Thus, the reduction in Volta potential difference and Volta potential gradient are two reasons for the protective effect offered by the molybdate inhibitor.

Weight-loss and electrochemical experiments were performed to further evaluate the corrosion inhibition effect of molybdates on AA6063-T5.

3.2.2.1. Weight loss tests. The long-term weight loss measurements of AA6063-T5 samples in 0.05 M NaCl solution with and without 3 mM of molybdate inhibitor were used as an indicator of how the corrosion rate changes with time, and the data are presented in Fig. 6a. The weight loss for the samples exposed to the chloride-containing electrolyte without inhibitor increased with increasing immersion time. The weight loss was significantly reduced in 0.05 M NaCl + 3 mM $(NH_4)_6Mo_7O_{24}$ solution. A pale-yellow-colored surface film was formed on the surface after several hours of exposure. The surface

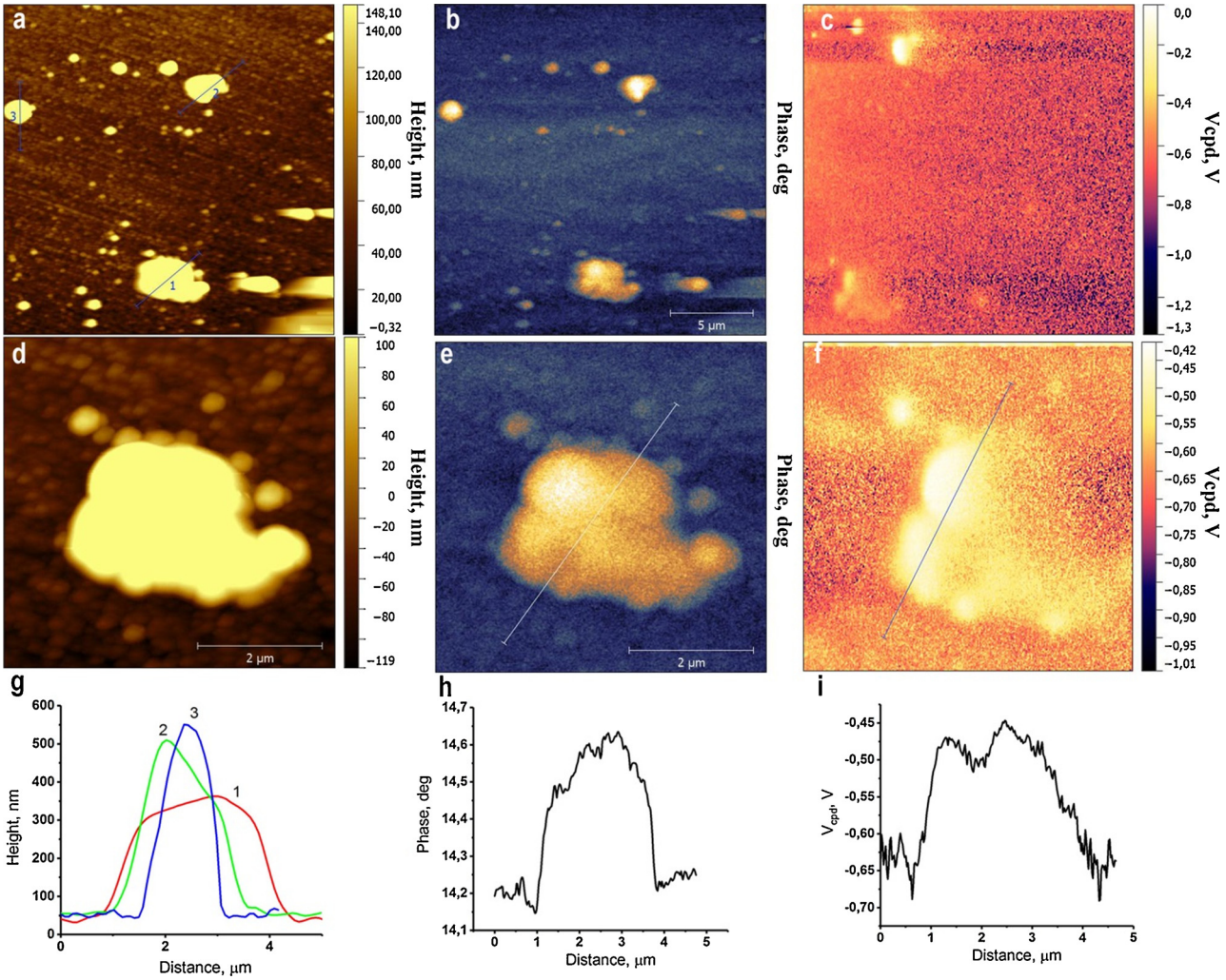

Fig. 5. Topography AFM maps (a, d) and corresponding MFM (b, e), and ImEFM Volta-potential maps (c, f) of AA6063-T5 surface after 4 h of exposure to 0.05 M NaCl + 3 mM $(NH_4)_6Mo_7O_{24}$. The line profiles show the topography and potential along the lines in the corresponding maps.

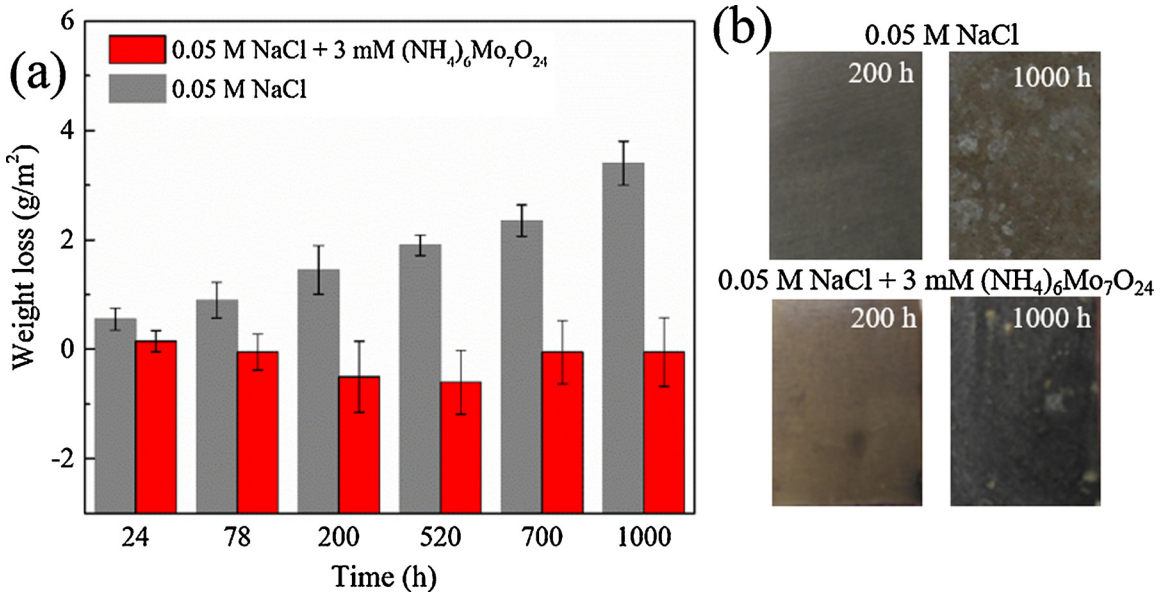

Fig. 6. Weight loss vs. time (a) and photographs of AA6063-T5 samples after immersion tests in 0.05 M NaCl with and without 3 mM $(NH_4)_6Mo_7O_{24}$ (b).

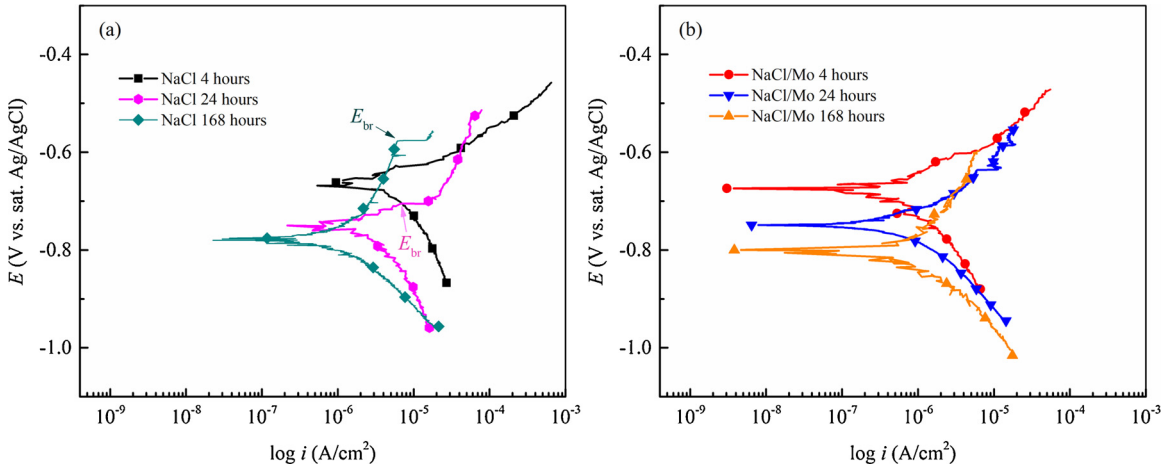

Fig. 7. Potentiodynamic polarization curves obtained after 4, 24, and 168 h exposure in 0.05 M NaCl without (a) and with 3 mM $(NH_4)_6Mo_7O_{24}$ (b). The scale in (a) and (b) is the same for the ease of comparison. The scan direction was from cathodic to anodic branch.

film became much thicker after 24 h of exposure and had a yellow-black color, turning totally black after ca. 100 h exposure (see Fig. 6b).

The data for samples exposed to 0.05 M NaCl containing molybdate inhibitor shows that after some initial loss, the mass of the samples increased slightly, thus resulting in negative values of the calculated weight loss. This is due to the formation of the conversion layer of the inhibitor on the alloy surface. The small increase in weight loss after 520 h of exposure is probably due to the initiation of corrosion. In this case, the results of the weight loss experiments cannot be used for a direct quantitative determination of the inhibition efficiency or direct correlation between the maximum pitting depth and weight loss [29]. Nevertheless, the effect of corrosion suppression exerted by molybdate is clear.

3.2.2.2. Potentiodynamic polarization measurements. Representative potentiodynamic polarization curves obtained after 4, 24, and 168 h of exposure of the AA6063-T5 samples in 0.05 M NaCl solutions with and without the molybdate inhibitor are shown in Fig. 7. After 4 h of exposure in the solution without inhibitor (Fig. 7a), active dissolution of the AA6063-T5 alloy was observed during anodic polarization. Longer exposure to the 0.05 M NaCl solution without the molybdate inhibitor resulted in a shift of the corrosion potential (E_{corr}) towards the cathodic region by 81 ± 18 and 109 ± 35 mV for 24 and 168 h of immersion, respectively. Moreover, the breakdown potential (E_{br}) can be distinguished at around −705 mV and −580 mV after 24 h and 168 h of immersion, respectively. This potential corresponds to the breakdown of the surface film of insoluble corrosion products, occurrence of which is clearly seen in Fig. 3, and results in reactivation of the pitting corrosion process. At the same time the corrosion current density, i_{corr}, decreased from 7.3 ± 0.6 μA/cm^2 after 4 h of immersion to, respectively, 3.6 ± 0.3 and 2.3 ± 0.3 μA/cm^2 after 24 and 168 h of exposure. This suggests a weak passivation of the alloy surface by insoluble corrosion products. However, the recorded i_{corr} values remained relatively high.

Polarization measurements in molybdate-containing NaCl solutions showed that the molybdate inhibitor provides a clear inhibition effect (Fig. 7b). In general, the values of E_{corr} in molybdate-containing solutions were 10–20 mV lower than those in the inhibitor-free solutions at the same exposure times. The extracted values of the corrosion current density were (5.0 ± 0.4), (1.8 ± 0.2), and (5.2 ± 0.5) × 10^{-7} A/cm^2 for 4, 24, and 168 h of exposure, respectively. The Tafel slopes of both the cathodic and anodic branches of the polarization curves changed in the presence of the inhibitor. These findings combined with a significant decrease in the corrosion current density suggest efficient passivation of the AA6063-T5 surface by molybdates, which provide mixed inhibition kinetics. The adsorbed molybdates initially impeded the anodic dissolution reaction occurring on active sites in the microstructure and retarded the cathodic oxygen reduction reaction occurring on micrometer-sized cathodic IMPs and passive regions of the alloy matrix.

Direct comparison of the polarization results in NaCl solution without and with inhibitor allowed calculation of the inhibition efficiency, *IE*, of the molybdate using Eq. (1) [4]:

$$IE = [1 - (i^{corr}/i^{0}_{corr})] \times 100\% \quad (1)$$

where i^{0}_{corr} and i_{corr} are the corrosion current densities in the absence and presence of the inhibitor, respectively. The calculated *IE* was ca. 93%, 94%, and 77% after 4, 24, and 168 h of exposure, respectively.

3.2.2.3. EIS analyses. Typical Nyquist plots of the EIS spectra obtained at different immersion times in 0.05 M NaCl solution without and with inhibitor are shown in Fig. 8. Nyquist plots for the samples after 10 min and 4 h of exposure to molybdate-free NaCl solution showed two time constants: a capacitive loop in the high and middle-frequency range and an inductive loop in the low-frequency range (Fig. 8a). The inductive behavior is suggested to arise from anodic processes occurring on the Al alloy surface [4,23,30]. The origin of the time constant in the low-frequency range changed from inductive to capacitive after 24 h of exposure, which is explained by the blocking effect of corrosion products adsorbed on the alloy surface and thus suppressing the active dissolution of the matrix. Further exposure to the corrosion medium resulted in an increase in the diameter of the semicircle. The EIS spectra obtained in the molybdate-containing solution did not show any inductive response and appeared as two consecutive capacitive loops (Fig. 8b). The obtained impedance values were significantly larger than in the case of 0.05 M NaCl solution without inhibitor (note the difference in scale in Fig. 8(a,b)), demonstrating an inhibition effect of the molybdates. The highest values of the surface resistance in the molybdate-containing solutions were achieved after 72 h of exposure. The following slight decrease in the surface resistance after 168 h of exposure indicates initiation of corrosion, likely resulting from the increased number of microcracks in the Mo-rich layer on the surface.

The EIS data were fitted using the equivalent circuits shown in Fig. 8c and the fit parameters are summarized in Table 2. In the used circuits R_s represents the resistance of the corrosive media between the Al alloy surface and the reference electrode; R_1 is the charge transfer resistance; CPE_1 is a constant phase element for double layer capacitance; L_1 is the inductance; R_L is the resistance of the adsorbed charged species; R_2 and CPE_2 are the resistance and capacitance of the surface film, respectively [4,31]. A constant phase element (CPE) was used in

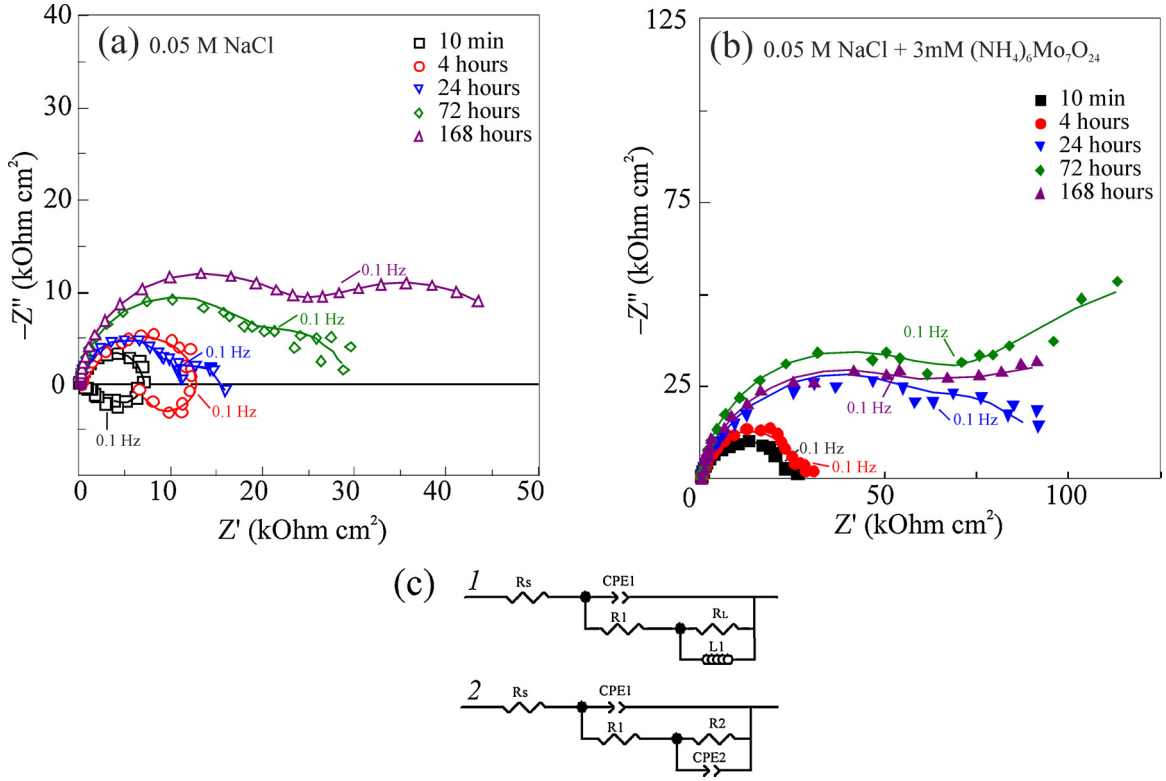

Fig. 8. Nyquist EIS plots in 0.05 M NaCl solution without (a) and with 3 mM $(NH_4)_6Mo_7O_{24}$ (b) during 168 h of exposure. The symbols correspond to experimental data and the lines are results of curve fitting. Equivalent circuits used for data analyzes are shown in (c).

the fitting analysis to represent the non-ideal capacitive response of the heterogeneous surfaces. From the EIS data, *IE* was calculated through the change in the charge transfer resistance [4]. The *IE* values calculated from the EIS data were in the range 68%–88%, depending on the immersion time. Two different equivalent circuits were used for the fitting of EIS spectra and caution should thus be taken for their direct comparison. The obtained IE values vary slightly depending on the applied method for parameter extraction as observed by comparing polarization and EIS results. In conclusion, the electrochemical experiments demonstrate good inhibition efficiency of molybdate toward suppression of AA6063-T5 corrosion, despite the slight difference in *IE* values calculated based on the two methods applied.

3.3. Surface film composition and inhibition mechanism

In order to gain a better understanding of the corrosion inhibition mechanism of AA6063-T5, it is essential to elucidate the valence and ionic forms of the molybdenum species formed in the solution and on the surface of the alloy during exposure to the corrosive solution. For that reason, theoretical calculations supported by Raman, UV-Vis, and XPS experiments were conducted.

3.3.1. Aqueous chemistry of molybdenum compounds

Fig. 9 shows fraction diagrams for molybdenum speciation calculated without any external potential corresponding to the initial aqueous conditions and by applying the OCP of AA6063-T5 immersed into 3 mM $(NH_4)_6Mo_7O_{24}$ solution to simulate conditions at the electrode/electrolyte interface. The diagram shown in Fig. 9a demonstrates that the MoO_4^{2-} ion predominates in the solution above pH 6 (the pH was about 7.2 in our solutions). The aqueous molybdate speciation is rather complex in the pH range 3–6. In this case, a series of protonated ions, namely $HMoO_4^-$, $HMo_7O_{24}^{5-}$, $H_2Mo_7O_{24}^{4-}$, and $H_3Mo_7O_{24}^{3-}$ are the predicted stable species. Further acidification results in the formation of the H_2MoO_4 acid, which is the only predicted compound at pH lower than ~3.

When the metal is immersed in the solution, several electrochemical

Table 2
Fitting data and calculated inhibition efficiency (*IE*) extracted from EIS measurements.

Exposure time (h)	R_s (Ω cm²)	R_1 (kΩ cm²)	Y_1 ($\Omega^{-1}cm^{-2}s^n$) × 10^6	n_1	R_2 (kΩ cm²)	Y_2 ($\Omega^{-1}cm^{-2}s^n$) × 10^6	n_2	L (kH cm²)	IE (%)
0.05 M NaCl									
0.17	190.0 ± 14.8	2.53 ± 0.12	6.53 ± 0.15	0.96 ± 0.03	4.63 ± 0.20	–	–	1987 ± 104	–
4	170.2 ± 16.1	5.65 ± 1.54	13.05 ± 1.66	0.84 ± 0.09	6.74 ± 0.32	–	–	24,428 ± 941	–
24	110.0 ± 16.3	10.59 ± 2.42	6.74 ± 0.61	0.95 ± 0.01	3.47 ± 0.22	34.38 ± 4.29	0.99 ± 0.01	–	–
72	126.0 ± 12.2	20.01 ± 3.59	8.45 ± 1.04	0.95 ± 0.01	9.31 ± 0.55	260.77 ± 22.76	0.88 ± 0.05	–	–
168	127.6 ± 16.4	25.12 ± 3.64	8.45 ± 0.99	0.95 ± 0.02	25.72 ± 2.67	180.83 ± 15.20	0.79 ± 0.10	–	–
0.05 M NaCl +3 mM $(NH_4)_6Mo_7O_{24}$									
0.17	8.96 ± 0.68	20.62 ± 2.54	6.78 ± 0.29	0.89 ± 0.03	3.48 ± 0.10	4.10 ± 0.14	0.95 ± 0.01	–	88
4	7.02 ± 0.64	32.47 ± 2.43	4.08 ± 1.05	0.99 ± 0.01	6.13 ± 0.33	2.87 ± 0.11	0.99 ± 0.01	–	83
24	200.1 ± 34.6	66.51 ± 4.68	1.01 ± 0.13	0.82 ± 0.05	21.74 ± 2.32	0.31 ± 0.18	0.99 ± 0.01	–	84
72	298.9 ± 28.4	83.21 ± 5.88	9.09 ± 0.56	0.87 ± 0.05	66.97 ± 3.85	0.11 ± 0.09	0.72 ± 0.09	–	76
168	300.4 ± 28.8	78.66 ± 6.61	6.41 ± 1.24	0.94 ± 0.02	165.62 ± 15.26	0.89 ± 0.12	0.73 ± 0.08	–	68

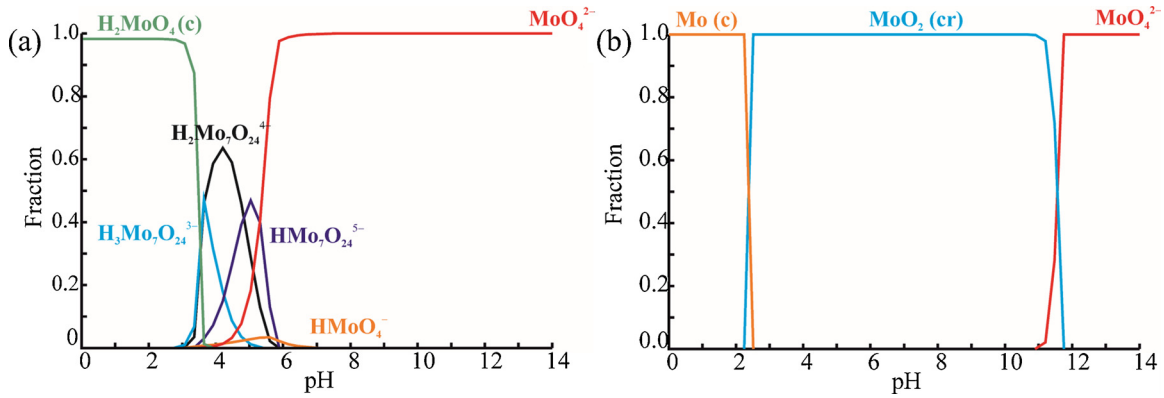

Fig. 9. Fraction diagrams for an aqueous solution prepared by dissolving 3 mM $(NH_4)_6Mo_7O_{24}$ and 0.05 M NaCl. Diagram (a) is calculated without any external potential, and (b) at $-0.450\ V_{SHE}$, the measured OCP of AA6063-T5.

reactions at the alloy surface and homogeneous chemical reactions in the liquid phase can take place due to the potential difference at the electrode/electrolyte interface which approaches ~ −0.67 V (sat. Ag/AgCl). At this potential molybdate species can be spontaneously reduced to the Mo(IV) oxide MoO_2 in the pH range ~2.5–11.8 and to metallic Mo at pH lower ~2.5. Thus, several oxidation-reduction processes involving Mo compounds can occur on the surface of AA6063-T5. Note that the OCP changes with time (Fig. 7) causing possible change in aqueous molybdate speciation. Fraction diagrams built for the OCP values after 24 h and 168h of immersion (Fig. S1 in the Supplementary information) revealed a shift of the Mo/MoO_2 equilibrium to a higher pH (~4.5).

3.3.2. *Raman spectroscopy*

The Raman spectra of the initial AA6063-T5 surface and after different immersion times are presented in Fig. 10a. The different spectra were acquired under ambient conditions at the different surface microstructural features (marked with arrows in Fig. 10(b,c)) after exposure to 0.05 M NaCl + 3 mM $(NH_4)_6Mo_7O_{24}$ solution for 4 and 24 h. As the most *d*-block high-valence metal, Mo can form numerous anionic complexes and solid oxides in aqueous solutions. The Raman peaks were interpreted by comparing the peak positions with those reported in the literature for various molybdenum compounds (Table 3) [32–40].

The Raman spectrum of as-polished AA6063-T5 showed no detectable Raman peaks (Fig. 10a, spectrum *1*) and no significant difference was observed after 4 h of immersion in 0.05 M NaCl without inhibitor (not shown). After 4 h of immersion in 0.05 M NaCl + 3 mM $(NH_4)_6Mo_7O_{24}$ solution, low-intensity and rather distorted Raman bands centered around 1039, 939, 863, 763, 618, and 448 cm^{-1} were acquired at several spots on the alloy surface (Fig. 10a, spectrum 2). These surface locations could be micrometer-sized IMPs with an overlayer of molybdates, consistent with data presented in Fig. 3. The positions of the main peaks in the spectrum differ from those reported in the literature (Table 3) and peak assignment should be carried out with care. As reported by Spevack and McIntyre [41], the ν_{sym} (Mo–O) band is used to identify the exact form of the molybdate species because of its highest intensity and sensitivity to changes in the coordination geometry, hydration degree, and degree of polymerization. This band shifts to higher frequencies as the oxidation state of Mo and degree of polymerization increase [36,41,42]. Further, the recorded broad Raman peaks are suggested to be due to the distortion of two-dimensional hydrated molybdenum structures on the surface [39,41]. Based on this, two bands at 939 and 863 cm^{-1} were assigned to symmetric and asymmetric stretches of the terminal Mo−O bond of the MoO_6 unit in hydrated $Mo_7O_{24}^{6-}$, respectively [39,40,42]. The Raman bands at 763, 448 and 350 cm^{-1} correspond to molybdenum compounds in lower valence states on the surface. Pure MoO_2 gives the most intense Raman band at around 740 cm^{-1} [32,36], while bands in the region 744–790 cm^{-1} have been reported for mixed-valence Mo(VI)–Mo(V), Mo(VI)–Mo(IV), and Mo(V)–Mo(IV) species [36,41,43,44]. No clear references for the Mo species with Raman bands at 1039 and 618 cm^{-1} were found in the literature. Nevertheless, a tentative assignment of these bands can be done [42]. As stated above, condensation of molybdates on the metal surface leads to the formation of surface polymolybdate structures. Minor distortion of the hydrated polymolybdate structures and their interaction with the alloy surface may result in a noticeable shift to higher Raman frequencies. Such a shift of up to 20 cm^{-1} was reported by Hu et al. for Mo-based catalysts [39], and also recently observed by Verbruggen et al. for molybdate-phosphate conversion coatings on steel [42]. Therefore, these bands are suggested to originate from large hydrated polyoxomolybdate clusters of unknown stoichiometry. To summarize, hydrated Mo(VI) polyoxomolybdates and mixed Mo(VI)/Mo(V) or Mo(VI)/Mo(IV) oxide compounds were identified on the surface after 4 h of exposure. In addition, a thin layer of adsorbed Mo species may be deposited on the Al matrix surface as discussed in the ImEFM measurements section, but if so, its thickness is not sufficient to allow detection by the Raman spectroscopy instrument used in this study.

After 24 h of exposure two typical appearances of the Raman spectra were found (Fig. 10a, spectra *3* and *4*). First, similar spectra to those measured after 4 h of exposure with Raman bands at 1048, 1039, 1007, 940, 913, 743, 621, and 446 cm^{-1} were acquired on the yellow-colored periphery areas of the formed conversion layer (Fig. 10c). Two maxima at 1048 and 1034 cm^{-1} are observed on the top of the main peak centered around 1042 cm^{-1} with a broad shoulder to ca. 1120 cm^{-1}. This indicates that at least two polyoxomolybdate species are present on the surface. Small sharp peaks at 1007 and 996 cm^{-1} were identified as MoO_3 [36], which is consistent with the yellow colour of the precipitate. A very weak band at 913 cm^{-1} was identified as the asymmetric stretching of MoO_4 units of Mo(VI) polyoxomolybdates [38]. The maximum intensity of the Raman band around 740 cm^{-1} was observed at slightly lower Raman shifts than after 4 h of exposure, indicating higher amount of Mo(IV) oxide compounds on the surface. This band is rather wide and can indicate low crystallinity of these compounds and possibly the presence of mixed-valence molybdenum species, similar to the observations after 4 h. The higher intensity of the Raman bands after 24 h exposure compared to those obtained after 4 h is due to a larger thickness of the formed layer.

Second, the Raman spectrum marked as *4* in Fig. 10a was obtained from the surface area covered by a visibly dark-coloured layer (Fig. 10c). This spectrum shows sharp Raman bands at 991, 819, 377, 333, 280, 144 cm^{-1}, which confirms high crystallinity of the compound, as well as weak bands at 1007, 970, 922, and 660 cm^{-1}. This spectrum is characteristic for hydrated molybdenum(VI) oxide, $MoO_3(H_2O)_3$ [32,36,40,42,45,46], with a slight shift of the main peak

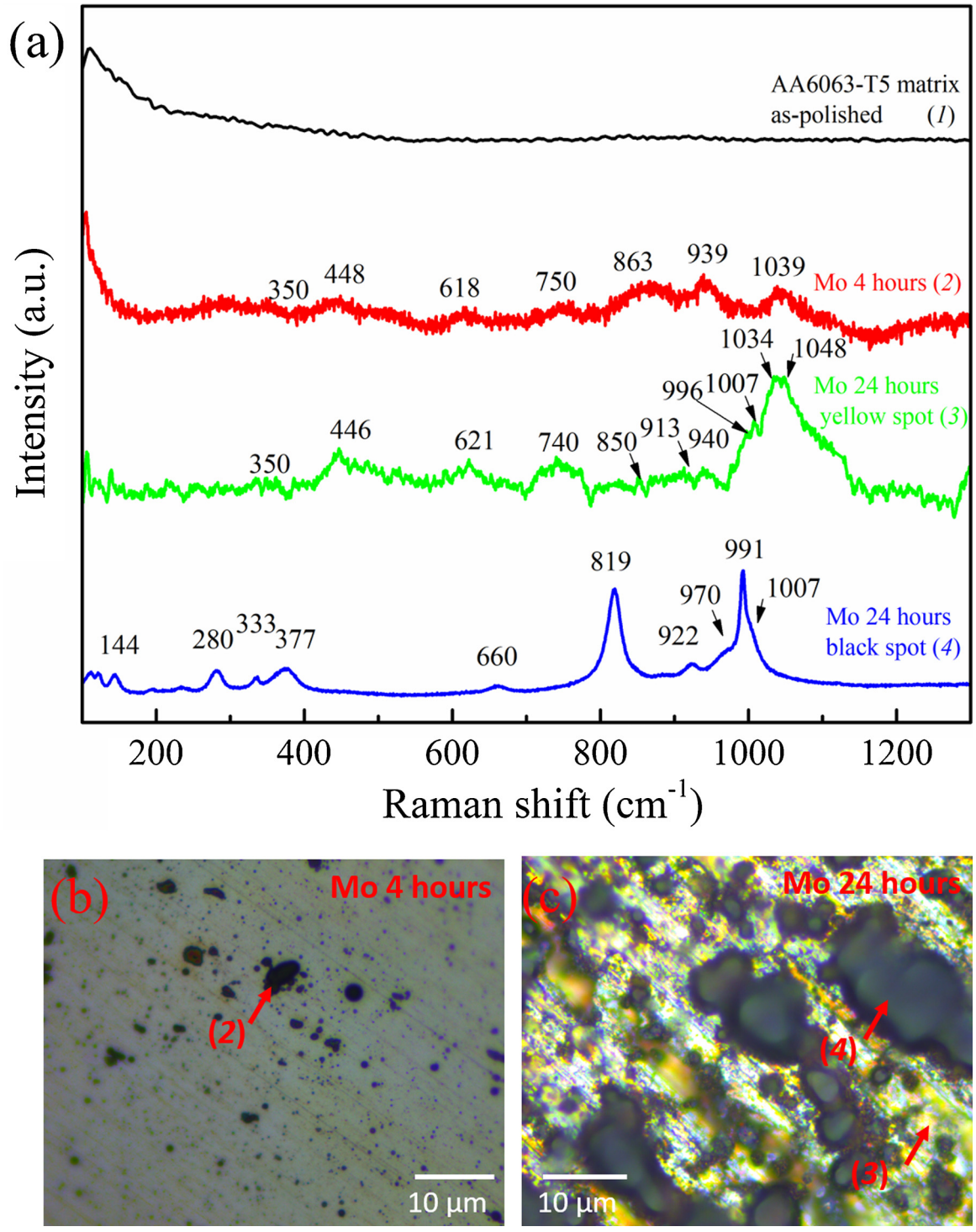

Fig. 10. Raman spectra of as-polished AA6063-T5 surface and typical microstructure features after exposure to 0.05 M NaCl solution with 3 mM $(NH_4)_6Mo_7O_{24}$. Optical micrographs (b, c) show surface areas where spectra (*2–4*) were acquired.

positions for the main bands. This is possibly due to reduction of the oxidization state of some Mo. The asignment is consistent with the dark colour of the surface precipitates [32,36,41,46]. The exact composition of this MoO_x intermediate oxide is speculative. A number of different mixed molybdenum oxides (Mo_4O_{11}, Mo_5O_{14}, $Mo_{17}O_{47}$, $Mo_{21}O_{61}$, etc.) have been reported in the literature [47,48]. However, there is a lack of reference Raman data for such compounds and their exact characterization is beyond the scope of the present study. Importantly, there are no Raman peaks around 740 cm^{-1}, which indicates the absence of pure Mo(IV) oxide in the examined spot and presence of mixed-valence compounds. Moreover, UV-Vis spectrum (Fig. S2 in the supplementary information) recorded after 24 h of exposure is characterized by a broad absorption wavelength domain, 200–400 nm, with the maxima at around 250 and 300 nm. The position and width of the absorption bands of polyoxomolybdates depend on the polymerization degree [49]. An increase in the number of Mo atoms in the oxoanions leads to a red shift of the band and its broadening. Comparison of the data obtained with the spectrum of bulk MoO_3 [50], provides some evidence that formation of a large fraction of pure MoO_3 on the surface of AA6063-T5 is unfavorable. This is essential for the corrosion inhibition

Table 3
Raman band positions (cm^{-1}) of solid (s) and aqueous (aq) molybdenum species.

Formula	Aggregate state	Band positions	Ref
Molybdenum(IV)			
m-MoO_2	s	201, 205, 227, 343, 346, 360, 422, 455, 466, 493, 567, 582, 737	[32]
m-MoO_2	s	203, 228, 345, 363, 461, 495, 571, 589, 744	[33]
Molybdenum(V)			
$MoOCl_5^{2-}$	aq	253, 372, 532, 742, 982 (1 M HCl) 378, 436, 802, 870, 984 (3–5 M HCl)	[34]
Molybdenum(VI)			
α-MoO_3	s	115, 129, 158, 198, 217, 245, 284, 291, 338, 365, 379, 472, 666, 820, 996, 1003	[32]
α-MoO_3	s	117, 130, 159, 199, 219, 244, 285, 293, 338, 368, 379, 470, 668, 821, 997	[33]
o-MoO_3	s	198, 218, 246, 270, 291, 302, 338, 374, 603, 666, 818, 820, 876, 990, 996	[35]
MoO_3	s	247, 284, 292, 339, 352, 367, 380, 469, 667, 822, 996, 1004	[36]
MoO_3	s	241, 284, 336, 376, 666, 821, 997	[37]
$Al_2(MoO_4)_3$	s	377, 434, 822, 889, 915, 993, 1004, 1026	[38]
MoO_4^{2-}	aq	317, 837, 897	[39]
$Mo_7O_{24}^{6-}$	aq	210, 362, 570, 903, 943	[39]
$Mo_7O_{24}^{6-}$	aq	220, 360, 860, 900, 937	[40]
$Mo_8O_{26}^{4-}$	aq	230, 370, 590, 925, 965	[39]

mechanism discussed below.

3.3.3. Post-immersion XPS analysis

The XPS analysis was performed in order to complement Raman experiments and elucidate the chemical states of Mo on the top surface of the AA6063-T5 alloy after 24 h of exposure to 0.05 M NaCl with 3 mM $(NH_4)_6Mo_7O_{24}$. High-resolution XPS spectra in the binding energy (BE) range of the Al*2p* and Mo*3d* peaks are presented in Fig. 11. The high-resolution Mo3*d* spectrum was deconvoluted into three peak doublets corresponding for Mo(VI) (232.7 ± 0.1 eV), Mo(V) (229.9 ± 0.1 eV), and Mo(IV) (229.2 ± 0.1 eV) compounds [41,42,51]. The relative Mo(VI) : Mo(V) : Mo(IV) ratio was 1 : 2.5 : 2.8. However, the peak assignment to specific Mo compounds is not straightforward. The reason is that Raman data suggest that not a single-phase but rather a mixture of different Mo compounds was formed on the surface. As stated in [42], several Mo compounds have the same or very similar BE. Thus, here we report only oxidation states of molybdenum in the surface layer of the AA6063-T5 alloy. The deconvolution of the Al2*p* high-resolution XPS spectra revealed doublets located in the energy range characteristic for metallic aluminum (72.5 eV), Al_2O_3 oxide (75.0 ± 0.2 eV), and AlO(OH) (76.1 eV), respectively. The results indicate that the passive/adsorption layer is rather thick because the Al metal peak is barely visible.

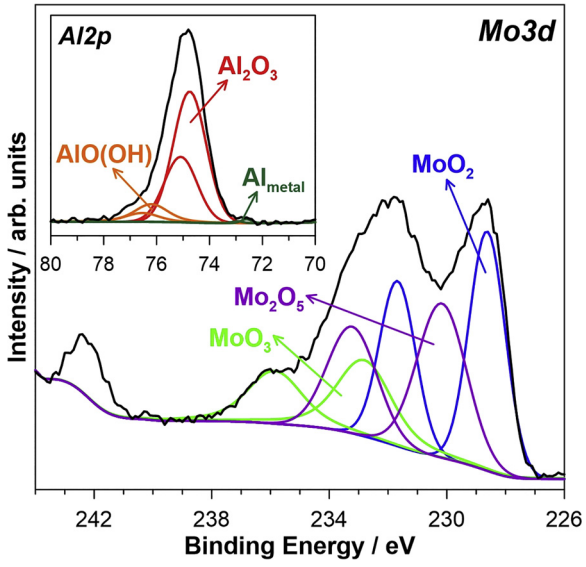

Fig. 11. High-resolution XPS spectra registered in the binding energy range of *Mo3d* and *Al2p* at the surface of the analyzed sample after immersion in 0.05 M NaCl + 3 mM $(NH_4)_6Mo_7O_{24}$ solution for 4 h. The black solid line represents experimental data, while deconvolution results are coloured lines.

3.3.4. Mechanism of inhibition

Our results demonstrate that molybdate belongs to the precipitation-inducing inhibitor class, forming a protective insoluble film on the metal surface. According to the electrochemical data (Figs. 7 and 8), molybdate provides mixed inhibition impeding both anodic and cathodic reactions. The surface analysis supports the occurrence of several oxidation-reduction processes involving molybdenum compounds on the surface of the AA6063-T5 alloy. This also indicates the importance of dissolved oxygen in the inhibition mechanism [9]. A thin hydrated film of aluminum oxide is formed over the Al matrix upon immersion of the alloy sample in the studied solution. In the case of the AA6063-T5 alloy, the large IMPs on the surface act as defect centers where a protective oxide film is not formed. The ImEFM data shown in Fig. 2 confirm that micrometer-sized IMPs in the AA6063-T5 structure are electrochemically cathodic relative to the Al matrix and the interphase boundaries are typically anodic. Reduction reactions will take place on cathodic regions of the surface, while oxidation will occur on anodic sites. This results in the initiation of localized corrosion in the boundary regions surrounding these IMPs [4,23,27,52].

When molybdate anions are present in the solution they will initially adsorb on the alloy surface due to its excess positive charge [12], followed by their spontaneous reduction to Mo(IV) species, as follows from the equation:

$$MoO_4^{2-} + 4H^+ + 2e^- \rightarrow MoO_2 + 2H_2O. \quad (2)$$

Here monomolybdate MoO_4^{2-} ions are assumed to be the only species present in the initial 0.05 M NaCl + 3 mM $(NH_4)_6Mo_7O_{24}$ solution as proposed by *Medusa* calculations (Fig. 9) and literature data [53]. Note that the reduction of initially adsorbed molybdate species was only considered over the oxide-free intermetallic particles, which is supported by the SEM/EDS observations (Fig. 4 where formation of a Mo-rich layer over Fe-rich large IMPs was demonstrated). The near-surface pH of the cathodic areas is higher than the bulk pH due to the OH^- ions formed during oxygen reduction. Oppositely, the local pH in the regions next to the cathodic IMPs can significantly decrease due to anodic dissolution of the Al matrix, which will supply H^+ ions for the above-mentioned reduction reaction [12,52]. Further, the importance of the initial corrosion attack for the precipitation of the protective layer of the molybdate inhibitor was observed. Reference experiments in the solution containing only 3 mM $(NH_4)_6Mo_7O_{24}$ without chloride ions showed that a thin molybdate surface film was formed after 24 h, and this layer was not able to provide reliable corrosion inhibition in salt spray or electrochemical tests. This correlates well with a low oxidizing capacity of Mo(VI) compounds in alkaline and near-neutral solutions [20].

The thermodynamic calculations (Fig. 9) suggest that at low pH the surface of the Al alloy should reduce the initial molybdate ions to metallic Mo. However, no strong evidence for the occurrence of this process was observed, which may suggest the presence of a kinetic hindrance [20]. The results reported in Fig. 9 corresponds to the thermodynamic equilibrium conditions, while the studied system is non-equilibrium but strives toward equilibrium. The formation of Mo(III) compounds was not considered since they were reported to be formed at more negative (~ −1.25–2.0 V (SCE)) potentials [15].

Overall, the results of this study, particularly the Raman data,

provide some evidence for a second step in the inhibition mechanism over cathodic IMPs. It includes subsequent oxidation of the reduced Mo (IV) species leading to the formation of mixed-valence molybdenum compounds. In the simplest case, mixed Mo(VI)/Mo(V) oxide can form as:

$$8MoO_2 + 6H_2O - 12e^- \rightarrow 2Mo_4O_{11} + 12H^+. \quad (3)$$

This process can occur through the formation of monomeric $MoO_2(OH)$ and dimeric $[Mo_2O_4(H_2O)_6]^{2+}$ oxomolybdenum(V) species which are later reduced to mixed-valence oxides [54]. As stated above, several compounds with different Mo(VI)/Mo(V) ratios could be formed on the surface, and non-stoichiometric mixed phases are observed in the Raman measurements, as shown in Fig. 10. Formation of a large fraction of Mo(VI) oxide was not considered since no strong support was found in the experimental data.

The next step in the inhibition mechanism is the polymerization of the adsorbed inhibitor layer. Local acidification due to the formation of H^+ in the vicinity of the corroding sites (Eq. (3)) causes local pH decrease. This will result in the polymerization of the adsorbed molybdenum species, and many different polyanions can be formed on the surface as follows from the presented Raman data in Fig. 10. It is not possible to exactly identify their stoichiometry due to the complex nature of the oligomerization processes in the acidic solutions containing molybdenum species [42,54]. Further condensation and local saturation of the surface with molybdenum species result in increased thickness of the film, which eventually causes the formation of crystalline hydrated mixed-valence molybdenum compounds. This was clearly observed in SEM and optical images in Figs. 4 and 10, and also detected with Raman spectroscopy. No clear sign of the presence of the polymerized molybdenum compounds over this crystalline layer was observed, possibly due to the low isoelectric point of the formed oxide layer, which makes further adsorption of molybdate ions unfavorable. No data on the isoelectric point of mixed Mo(VI)/Mo(V) oxides was found in the literature, but it is expected to be much lower than the pH in the region near cathodic IMPs [55].

The inhibition mechanism over the oxide-covered alloy matrix is different and does not involve the described oxidation-reduction processes of molybdenum species. In that case, the Al matrix is passivated in the studied solution and an oxide layer is formed on the surface. The high isoelectric point of the oxide-covered matrix (around 9.5) supports adsorption of anions, including molybdates. However, the low cathodic activity of Al_2O_3 does not promote the initial reduction of the adsorbed Mo(VI) species, thus the presence of only polymerized Mo(VI) is favourable. The SEM and Raman results presented in Figs. 4 and 10 demonstrate that formation of the protective molybdenum-containing surface film is not limited to only IMPs, as, for example, reported by Lopez-Garrity and Frankel for the AA2024-T3 alloy [9]. On the contrary, the continuous growth of a thick passivating film over the surface was observed for the AA6063-T5 alloy. The periphery area of the passive film acts as a propagation site for the film growth. Most probably, additional disproportionation and/or comproportionation redox reactions are taking place in regions between polymerized Mo(VI) species, covering the Al matrix surface, and mix-valence molybdenum compounds in the crystalline layer. Another possible mechanism can be connected with the corrosion of the Al matrix in the periphery of the passivated IMPs, causing a local change in the pH and promoting redox processes similar to Eq. (2). Accordingly, the corrosion will be suppressed by the film formed.

The comparison of the results reported in this manuscript with those on the vanadate inhibitor reported previously [4,12,31], gives evidence that molybdate and vanadate have similar protection efficiency (EI = 93–95% during one-day tests) for suppression of AA6063-T5 corrosion. The inhibitive action of both inhibitors is strongly associated with cathodic IMPs in the microstructure of the alloy. However, in the case of molybdate, an almost uniform conversion layer was formed on the surface, which was not typical for vanadate. The mechanisms of corrosion inhibition of AA6063-T5 provided by these inhibitors are similar in the sense that in both cases it includes two-stage oxidation-reduction processes occurring on the top of cathodic IMPs. Importantly, the molybdate has lower toxicity and is possibly more favourable from the ecological perspective.

4. Conclusions

In this work, we studied the effect of molybdate on the corrosion properties of the aluminum AA6063-T5 alloy. The electrochemical data were correlated with the microstructure of the alloy and the composition of the Mo-rich layer. The following conclusions are drawn:

1 The microstructure of AA6063-T5 includes numerous micrometer-sized IMPs. ImEFM measurements demonstrated the electrochemical cathodic nature of IMPs, resulting in a high susceptibility to micro-galvanic corrosion between the Al matrix and IMPs.
2 Electrochemical data revealed that the addition of 3 mM $(NH_4)_6Mo_7O_{24}$ in aqueous 0.05 M NaCl solution leads to a significant decrease in the corrosion rate of the AA6063-T5 alloy. Molybdate provides mixed corrosion inhibition effects with inhibition efficiency of about 90% within 1 day of exposure.
3 Surface analysis indicated that the initiation of the inhibition process occurs over micrometer-sized cathodic IMPs. The resulting surface film consists of two characteristic areas: black area (containing Mo(V) and Mo(VI) compounds) surrounded by a yellow periphery region of (Mo(IV), Mo(V), and Mo(VI) compounds). The former consisted of crystalline compounds, while the latter contained a large fraction of amorphous polymerized species.
4 The mechanism of corrosion inhibition of AA6063-T5 by $(NH_4)_6Mo_7O_{24}$ in aqueous 0.05 M NaCl solution follows several stages, with initial reduction of the adsorbed Mo(VI) species over cathodic IMPs to Mo(IV), promoted by corrosion of the Al matrix in the vicinity of those IMPs, following by a subsequent oxidization with formation of mixed-valence Mo(V) and Mo(VI) compounds. The surface of the Al matrix does not support such a redox mechanism of inhibition due to its low electrochemical activity.

Data availability

The raw/processed data required to reproduce these findings cannot be shared at this time as the data also forms part of an ongoing study.

CRediT authorship contribution statement

Dmitry S. Kharitonov: Conceptualization, Methodology, Investigation, Data curation, Formal analysis, Visualization, Validation, Funding acquisition, Writing - original draft. **Illia Dobryden:** Conceptualization, Methodology, Investigation, Visualization, Formal analysis, Writing - review & editing. **Birhan Sefer:** Investigation. **Jacek Ryl:** Investigation, Formal analysis. **Angelika Wrzesińska:** Investigation. **Irina V. Makarova:** Investigation. **Izabela Bobowska:** Investigation. **Irina I. Kurilo:** Project administration, Supervision, Funding acquisition, Writing - review & editing. **Per M. Claesson:** Conceptualization, Supervision, Validation, Writing - review & editing.

Declaration of Competing Interest

The authors declare that they have no known competing financial interests or personal relationships that could have appeared to influence the work reported in this paper.

Acknowledgements

Dmitry Kharitonov gratefully acknowledges financial support from

the Si Swedish Institute (Visby programme scholarship) and Erasmus + mobility program. Irina Kurilo gratefully acknowledges The Ministry of Education of the Republic of Belarus for financial support under grant no. 20192322 “Composite oxide coatings on aluminum matrix with enhanced physic-chemical and anticorrosion properties”. Jacek Ryl gratefully acknowledges the financial support of the Polish Ministry of Science and Higher Education from the budget funds in the period 2016–2019 under Iuventus Plus project no. IP2015067574.

Appendix A. Supplementary data

Supplementary material related to this article can be found, in the online version, at doi:https://doi.org/10.1016/j.corsci.2020.108658.

References

[1] Z. Szklarska-Smialowska, Pitting corrosion of aluminum, Corros. Sci. 41 (1999) 1743–1767, https://doi.org/10.1016/S0010-938X(99)00012-8.
[2] G.M. Scamans, N. Birbilis, R.G. Buchheit, Corrosion of aluminum and its alloys, Shreir’s Corros. (2010) 1974–2010, https://doi.org/10.1016/B978-044452787-5.00095-0.
[3] Y. Zhu, K. Sun, G.S. Frankel, Intermetallic phases in aluminum alloys and their roles in localized corrosion, J. Electrochem. Soc. 165 (2018) C807–C820, https://doi.org/10.1149/2.0931811jes.
[4] D.S. Kharitonov, C. Örnek, P.M. Claesson, J. Sommertune, I.M. Zharskii, I.I. Kurilo, J. Pan, Corrosion inhibition of aluminum alloy AA6063-T5 by vanadates : microstructure characterization and corrosion analysis, J. Electrochem. Soc. 165 (2018) C116–C126, https://doi.org/10.1149/2.0341803jes.
[5] Y. Zhu, K. Sun, J. Garves, L.G. Bland, J. Locke, J. Allison, G.S. Frankel, Micro- and nano-scale intermetallic phases in AA2070-T8 and their corrosion behavior, Electrochim. Acta 319 (2019) 634–648, https://doi.org/10.1016/j.electacta.2019.05.028.
[6] J. Zhao, L. Xia, A. Sehgal, D. Lu, R.L. McCreery, G.S. Frankel, Effects of chromate and chromate conversion coatings on corrosion of aluminum alloy 2024-T3, Surf. Coatings Technol. 140 (2001) 51–57, https://doi.org/10.1016/S0257-8972(01)01003-9.
[7] M.W. Kendig, R.G. Buchheit, Corrosion inhibition of aluminum and aluminum alloys by soluble chromates, chromate coatings, and chromate-free coatings, Corrosion. 59 (2003) 379–400, https://doi.org/10.5006/1.3277570.
[8] O. Gharbi, S. Thomas, C. Smith, N. Birbilis, Chromate replacement: what does the future hold? NPJ Mater. Degrad. 2 (2018) 12, https://doi.org/10.1038/s41529-018-0034-5.
[9] O. Lopez-Garrity, G.S. Frankel, Corrosion inhibition of aluminum alloy 2024-T3 by sodium molybdate, J. Electrochem. Soc. 161 (2013) C95–C106, https://doi.org/10.1149/2.044403jes.
[10] S.B. Madden, J.R. Scully, Inhibition of AA2024-T351 corrosion using permanganate, J. Electrochem. Soc. 161 (2014) C162–C175, https://doi.org/10.1149/2.075403jes.
[11] K. Dychtoń, P. Kwolek, The replacement of chromate by molybdate in phosphoric acid-based etch solutions for aluminium alloys, Corros. Eng. Sci. Technol. 53 (2018) 234–240, https://doi.org/10.1080/1478422X.2018.1446582.
[12] D.S. Kharitonov, J. Sommertune, C. Örnek, J. Ryl, I.I. Kurilo, P.M. Claesson, J. Pan, Corrosion inhibition of aluminium alloy AA6063-T5 by vanadates: local surface chemical events elucidated by confocal Raman micro-spectroscopy, Corros. Sci. 148 (2019) 237–250, https://doi.org/10.1016/j.corsci.2018.12.011.
[13] K.D. Ralston, S. Chrisanti, T.L. Young, R.G. Buchheit, Corrosion inhibition of aluminum alloy 2024-T3 by aqueous vanadium species, J. Electrochem. Soc. 155 (2008) C350–C359, https://doi.org/10.1149/1.2907772.
[14] D. Schamphelaere, et al., The chronic toxicity of molybdate to freshwater organisms. I. Generating reliable effects data, Sci. Total Env. 408 (2010) 5362–5371, https://doi.org/10.1016/j.scitotenv.2010.07.041.
[15] K.C. Emregül, A.A. Aksüt, The effect of sodium molybdate on the pitting corrosion of aluminum, Corros. Sci. 45 (2003) 2415–2433, https://doi.org/10.1016/S0010-938X(03)00097-0.
[16] C.B. Breslin, G. Treacy, W.M. Carroll, Studies on the passivation of aluminium in chromate and molybdate solutions, Corros. Sci. 36 (1994) 1143–1154, https://doi.org/10.1016/0010-938X(94)90139-2.
[17] G. Wang, M. Zhang, R. Wu, Molybdate and molybdate/permanganate conversion coatings on Mg-8.5Li alloy, Appl. Surf. Sci. 258 (2012) 2648–2654, https://doi.org/10.1016/j.apsusc.2011.10.112.
[18] Y. Huang, S. Mu, Q. Guan, J. Du, Corrosion resistance and formation analysis of a molybdate conversion coating prepared by alkaline treatment on aluminum alloy 6063 a b c d, J. Electrochem. Soc. 166 (2019) C224–C230, https://doi.org/10.1149/2.1111908jes.
[19] W.C. Moshier, G.D. Davis, Interaction of molybdate anions with the passive film on aluminum, Corrosion. 46 (1990) 43–50, https://doi.org/10.5006/1.3585065.
[20] V. Shkirskiy, P. Keil, H. Hintze-Bruening, F. Leroux, T. Stimpfling, D. Dragoe, K. Ogle, P. Volovitch, $MoO^{4}2^{-}$ as a soluble inhibitor for Zn in neutral and alkaline solutions, Corros. Sci. 99 (2015) 31–41, https://doi.org/10.1016/j.corsci.2015.05.005.
[21] C. Monticelli, G. Brunoro, A. Frignani, G. Trabanelli, Evaluation of corrosion inhibitors by electrochemical noise analysis, J. Electrochem. Soc. 139 (1992) 706–711.
[22] M.A. Jakab, F. Presuel-Moreno, J.R. Scully, Critical concentrations associated with cobalt, cerium and molybdenum inhibition of AA2024-T3 corrosion: delivery from AL-CO-CE(-MO) alloys, Proc. Electrochem. Soc. 23 (2003) 236–254.
[23] D.S. Kharitonov, I.B. Dobryden, B. Sefer, I.M. Zharskii, P.M. Claesson, I.I. Kurilo, Corrosion of AD31 (AA6063) alloy in chloride-containing solutions, Prot. Met. Phys. Chem. Surf. 54 (2018) 291–300, https://doi.org/10.1134/S2070205118020077.
[24] R. Borgani, D. Forchheimer, J. Bergqvist, P.-A. Thorén, O. Inganäs, D.B. Haviland, Intermodulation electrostatic force microscopy for imaging surface photo-voltage, Appl. Phys. Lett. 105 (2014) 143113, https://doi.org/10.1063/1.4897966.
[25] D. Platz, E.A. Thoĺn, D. Pesen, D.B. Haviland, Intermodulation atomic force microscopy, Appl. Phys. Lett. 92 (2008), https://doi.org/10.1063/1.2909569.
[26] C. Örnek, M. Liu, J. Pan, Y. Jin, C. Leygraf, Volta potential evolution of intermetallics in aluminum alloy microstructure under thin aqueous adlayers: a combined DFT and experimental study, Top. Catal. 61 (2018) 1169–1182, https://doi.org/10.1007/s11244-018-0939-9.
[27] L. Yin, Y. Jin, C. Leygraf, N. Birbilis, J. Pan, Numerical simulation of micro-galvanic corrosion in Al alloys: effect of geometric factors, J. Electrochem. Soc. 164 (2017) C75–C84, https://doi.org/10.1149/2.1221702jes.
[28] H. Gruber, H. Haselmair, H.P. Fritzer, On magnetic properties of some molybdenum oxides, J. Solid State Chem. 47 (1983) 84–91, https://doi.org/10.1016/0022-4596(83)90045-2.
[29] S. Gioacchino, S. Gioacchino, The resistance of aluminium to atmospheric corrosion, Corros. Alum. (2004) 277–291, https://doi.org/10.1016/B978-0-08-044495-6.50021-5.
[30] D.S. Kharitonov, I.I. Kurilo, I.M. Zharskii, Effect of sodium vanadate on corrosion of AD31 aluminum alloy in acid media, Russ. J. Appl. Chem. 90 (2017) 1089–1097, https://doi.org/10.1134/S1070427217070102.
[31] D.S. Kharitonov, I.I. Kurilo, A. Wrzesinska, I.M. Zharskii, Corrosion inhibition of AA6063 alloy by vanadates in alkaline media, Mat.Wiss. u. Werkstofftech. 48 (2017) 646–660, https://doi.org/10.1002/mawe.201600752.
[32] M.A. Camacho-López, L. Escobar-Alarcón, M. Picquart, R. Arroyo, G. Córdoba, E. Haro-Poniatowski, Micro-Raman study of the m-MoO_2 to α-MoO_3 transformation induced by cw-laser irradiation, Opt. Mater. (Amst). 33 (2011) 480–484, https://doi.org/10.1016/j.optmat.2010.10.028.
[33] P.A. Spevack, N.S. McIntyre, Thermal reduction of molybdenum trioxide, J. Phys. Chem. 96 (1992) 9029–9035, https://doi.org/10.1021/j100201a062.
[34] S. Himeno, M. Hasegawa, Raman studies on molybdenium(V) species in HCl solutions, Inorganica Chim. Acta 83 (1984) L17–L18, https://doi.org/10.1016/S0020-1693(00)82362-2.
[35] L. Seguin, M. Figlarz, R. Cavagnat, J.C. Lassègues, Infrared and Raman spectra of MoO_3 molybdenum trioxides and MoO_3 xH_2O molybdenum trioxide hydrates, Spectrochim. Acta Part A Mol. Biomol. Spectrosc. 51 (1995) 1323–1344, https://doi.org/10.1016/0584-8539(94)00247-9.
[36] M. Dieterle, G. Mestl, Raman spectroscopy of molybdenum oxides: part II. Resonance Raman spectroscopic characterization of the molybdenum oxides Mo_4O_{11} and MoO_2, Phys. Chem. Chem. Phys. 4 (2002) 822–826, https://doi.org/10.1039/b107046k.
[37] K. Routray, W. Zhou, C.J. Kiely, W. Grünert, I.E. Wachs, Origin of the synergistic interaction between MoO_3 and iron molybdate for the selective oxidation of methanol to formaldehyde, J. Catal. 275 (2010) 84–98, https://doi.org/10.1016/j.jcat.2010.07.023.
[38] H. Tian, I.E. Wachs, L.E. Briand, Comparison of UV and visible Raman spectroscopy of bulk metal molybdate and metal vanadate catalysts, J. Phys. Chem. B 109 (2005) 23491–23499, https://doi.org/10.1021/jp053879j.
[39] H. Hu, I.E. Wachs, S.R. Bare, Surface structures of supported molybdenum oxide catalysts: characterization by Raman and Mo L3-Edge XANES, J. Phys. Chem. 99 (1995) 10897–10910.
[40] E. Payen, J. Grimblot, S. Kasztelan, Study of oxidic and reduced alumina-supported molybdate and heptamolybdate species by in situ laser Raman spectroscopy, J. Phys. Chem. 91 (1987) 6642–6648, https://doi.org/10.1021/j100311a018.
[41] P.A. Spevack, N.S. McIntyre, A Raman and XPS investigation of supported molybdenum oxide thin films. 1. Calcination and reduction studies, J. Phys. Chem. 97 (1993) 11020–11030, https://doi.org/10.1021/j100144a020.
[42] H. Verbruggen, K. Baert, H. Terryn, I. De Graeve, Molybdate-phosphate conversion coatings to protect steel in a simulated concrete pore solution, Surf. Coatings Technol. 361 (2019) 280–291, https://doi.org/10.1016/j.surfcoat.2018.09.056.
[43] B. Botar, A. Ellern, P. Kögerler, Mapping the formation areas of giant molybdenum blue clusters: a spectroscopic study, Dalton Trans. 41 (2012) 8951–8959, https://doi.org/10.1039/c2dt30661a.
[44] N. Mironova-Ulmane, A. Kuzmin, M. Grube, Raman and infrared spectromicroscopy of manganese oxides, J. Alloys. Compd. 480 (2009) 97–99, https://doi.org/10.1016/j.jallcom.2008.10.056.
[45] S. Patnaik, G. Swain, K.M. Parida, Highly efficient charge transfer through a double Z-scheme mechanism by a Cu-promoted MoO_3/g-C_3N_4 hybrid nanocomposite with superior electrochemical and photocatalytic performance, Nanoscale 10 (2018) 5950–5964, https://doi.org/10.1039/c7nr09049h.
[46] R. Murugan, A. Ghule, C. Bhongale, H. Chang, Thermo-Raman investigations on structural transformations in hydrated MoO_3, J. Mater. Chem. 10 (2000) 2157–2162, https://doi.org/10.1039/b000811g.
[47] M. Maciejewski, A. Baiker, A. Reller, Chemical and structural transformations in the system Mo/MoO/In reducing and oxidizing atmospheres, Solid State Ion. 43 (1990) 203–215, https://doi.org/10.1016/0167-2738(90)90485-A.
[48] M.A. Camacho-López, L. Escobar-Alarcón, E. Haro-Poniatowski, Structural transformations in MoOx thin films grown by pulsed laser deposition, Appl. Phys. A

Mater. Sci. Process. 78 (2004) 59–65, https://doi.org/10.1007/s00339-003-2235-0.
[49] K. Chen, S. Xie, E. Iglesia, A.T. Bell, Structure and properties of zirconia-supported molybdenum oxide catalysts for oxidative dehydrogenation of propane, J. Catal. 189 (2000) 421–430, https://doi.org/10.1006/jcat.1999.2720.
[50] C. Thomazeau, V. Martin, P. Afanasiev, Effect of support on the thermal decomposition of $(NH_4)_6Mo_7O_{24}{\cdot}4H_2O$ in the inert gas atmosphere, Appl. Catal. A Gen. 199 (2000) 61–72, https://doi.org/10.1016/S0926-860X(99)00523-2.
[51] J.G. Choi, L.T. Thompson, XPS study of as-prepared and reduced molybdenum oxides, Appl. Surf. Sci. 93 (1996) 143–149, https://doi.org/10.1016/0169-4332(95)00317-7.
[52] O. Guseva, J.A. Derose, P. Schmutz, Modelling the early stage time dependence of localised corrosion in aluminium alloys, Electrochim. Acta 88 (2013) 821–831, https://doi.org/10.1016/j.electacta.2012.10.059.
[53] E.A. Nagul, I.D. McKelvie, P. Worsfold, S.D. Kolev, The molybdenum blue reaction for the determination of orthophosphate revisited: opening the black box, Anal. Chim. Acta 890 (2015) 60–82, https://doi.org/10.1016/j.aca.2015.07.030.
[54] K.-H. Tytko, Gmelin Handbook of Inorganic Chemistry, Mo Molybdenum, Springer Berlin Heidelberg, 1986, https://doi.org/10.1007/978-3-662-0.
[55] M. Kosmulski, Isoelectric points and points of zero charge of metal (hydr)oxides: 50 years after Parks' review, Adv. Colloid Interface Sci. 238 (2016) 1–61, https://doi.org/10.1016/j.cis.2016.10.005.